RESEARCH ARTICLE

A nonlocal interface approach to peridynamics exemplified by continuum-kinematics-inspired peridynamics

Marie Laurien[1] | **Ali Javili**[2] | **Paul Steinmann**[1]

[1]Institute of Applied Mechanics, Friedrich-Alexander-Universität Erlangen-Nürnberg, Erlangen, Germany

[2]Department of Mechanical Engineering, Bilkent University, Ankara, Turkey

Correspondence
Marie Laurien, Institute of Applied Mechanics, Friedrich-Alexander-Universität Erlangen-Nürnberg, Egerlandstraße 5, 91058 Erlangen, Germany.
Email: marie.laurien@fau.de

Funding information
Deutsche Forschungsgemeinschaft, Grant/Award Number: 377472739; Scientific and Technological Research Council of Turkey (TÜBITAK), Grant/Award Number: 218M700

Abstract

In this contribution, we present a novel approach on how to treat material interfaces in nonlocal models based on peridynamics (PD) and in particular continuum-kinematics-inspired peridynamics (CPD), a novel variationally consistent peridynamic formulation. Our method relies on a nonlocal interface where the material subdomains overlap. Within this region, a kinematic coupling of the two constituents is enforced. The contact is purely geometrical as interaction forces act only between points of the same material. We provide a detailed description of the computational implementation within the framework of CPD, that is in principle applicable to all formulations of PD. A variety of numerical examples for modeling bimaterial interfaces illustrate the utility of the technique for both two-dimensional and three-dimensional problems, including examples at large deformations. Our model approaches a local model when the nonlocality parameter, the horizon size, is decreased. The proposed methodology offers a viable alternative to previous approaches in PD, which are essentially imposing mixture rules for the interfacial material parameters.

KEYWORDS

continuum kinematics, material interface, nonlocality, peridynamics

1 | INTRODUCTION

Peridynamics (PD) is a nonlocal continuum formulation that was introduced by Silling in 2000.[1] Providing a tool to describe long-range forces within a continuum framework, the theory is increasingly applied to model physical phenomena that are not accurately captured through the consideration of local contact forces in classical (local) continuum models. This is achieved by incorporating integral terms into the governing equations of PD that comprise the interaction forces acting across a finite distance. Thus, PD enriches a continuum model by including long-range interactions. Conceptually speaking, PD borrows certain concepts from both classical continuum mechanics (CCM) and molecular dynamics (MD). Due to the replacement of spatial derivatives with integral operators, PD is inherently capable of modeling discontinuities, such as cracks, within a continuum framework. It is therefore widely used in fracture mechanics,[2] but has expanded to a multitude of application fields, such as multiscale modeling,[3-7] multiphysics,[8-10] and biological systems.[11-14] In the basic version of PD, that is, bond-based PD, the Poisson ratio is restricted to $v = 1/4$ in three-dimensional

problems and $v = 1/3$ in two-dimensional problems. Consequently, Silling et al.[15] later extended the theory by introducing the so-called "state" that allows for a more sophisticated description of the interactions. Hence, in state-based PD, a point is influenced by the collective deformation of its neighborhood. An alternative approach is continuum-kinematics-inspired peridynamics (CPD) introduced by Javili et al.[16] very recently. Here, in addition to pair-wise interactions, multi-neighbor interactions characterize the interplay of points via a kinematically exact description. In this manner, it is possible to capture changes not only in length, but also in area and volume. This yields an intuitive description of the kinematics since the basic kinematic ingredients are inspired by those of classical continuum kinematics. As a consequence, CPD is able to model Poisson-like effects with Poisson's ratio v ranging between -1 and 0.5 (in 3D). CPD differs from state-based PD, which faces issues when transferring local material models to peridynamic ones via a correspondence model — a concept that state-based PD commonly relies on.[17] Due to these promising benefits, CPD has been further developed by now.[18-24]

In most real-world problems, materials are heterogeneous. Numerous fields of applications of PD are concerned with modeling heterogeneous media, such as micro-structured materials,[6,7] functionally graded materials,[25-28] or bilayers,[29] to name a few. This requires methodological approaches on how to treat material interfaces that are inherently nonlocal within a peridynamic model. In the literature, there exist very few contributions that have established a mathematical framework for nonlocal interface models.[30-32] Alali et al.[30] showed that in the presence of a material interface, neither the bond-based nor the state-based linear PD model converge to local elasticity for vanishing nonlocality. Therefore, nonlocal interface conditions were introduced together with a new nonlocal operator that acts on points in an extended interface. The practical implementation of PD material interfaces is, however, usually carried out in a simpler way, often based on empirical arguments. Silling et al.[15] include weighting functions into the computation of the force state that vanish for points outside the respective material. Commonly, the focus is on introducing additional peridynamic material constants that describe the bonds that are connecting dissimilar materials. A comparison can be drawn to MD, where intermolecular forces between unlike molecules are to be computed. There, the material parameters are combined according to mixture rules, also called combining rules, of which a multitude of variants exists.[33,34] Several similar approaches are followed in PD literature. A widespread method is to characterize an interfacial bond by simply averaging the parameters of the constituent materials.[25,26,28] Oftentimes, the parameters are weighted with the fraction of the bond length associated with the respective material. These approaches can further be classified into arithmetic averaging[6,35-37] and harmonic averaging.[6,7,9,38] Cheng et al.[26] used the proportion of the material coefficients to identify a weighting factor. Meanwhile, a couple of contributions introduced more freely selectable weighting factors.[29,39,40] Recently, Ahmadi et al.[41] determined the parameters by considering both the distance to the interface and the number of neighboring points of dissimilar material. Behera et al.[37] employed a Heaviside function to assign the parameters. Kilic et al.[42] consistently used the smaller bulk modulus based on results of numerical experimentation. Recently, Nguyen et al.[43] concluded from a comparison of four different methods that the results obtained from a harmonic mean including a weighting with the bond length fraction are the closest to a local interface with FEM. In summary, although PD inherently allows for material discontinuities, there remains an uncertainty in PD literature regarding an interface mixture rule. The choice of a specific mixture rule seems arbitrary to some extent. It might be due to the lack of extensive comparative studies that no consistent approach for PD interfaces exists. In most works, a local model serves to validate the results, even though a nonlocal model naturally behaves differently. On the other hand, it is difficult to obtain experimental data of the interfacial properties, that could support evaluating the mixture rules. Ultimately, in existing PD interface models, the material interface remains a two-dimensional discontinuity surface, as in a local model, while nonlocality manifests itself through interactions across the interface. However, the opposite approach has never been considered in this context, to the best of our knowledge. Therefore, we propose a model where nonlocality translates into a finite thickness interface region. Within this region, the dissimilar materials are kinematically enslaved. Peridynamic interaction forces, however, are present only within the same material. In this fashion, the question of an appropriate mixture rule is entirely by-passed. This is especially useful in CPD, where the use of a mixture rule is not straightforward. Within the scope of this work, this novel approach for nonlocal interfaces is introduced and investigated. For the first time CPD is utilized to model bimaterial interface problems.

This article is organized as follows. Section 2 introduces the theoretical framework of continuum-kinematics-inspired peridynamics. The conceptual idea and the computational implementation of the proposed nonlocal interface model are presented in Section 3. Numerical experiments in Section 4 demonstrate its applicability to a variety of two-dimensional and three-dimensional bimaterial models, including a nonlocality study with a comparison to a local interface. Section 5 concludes this work.
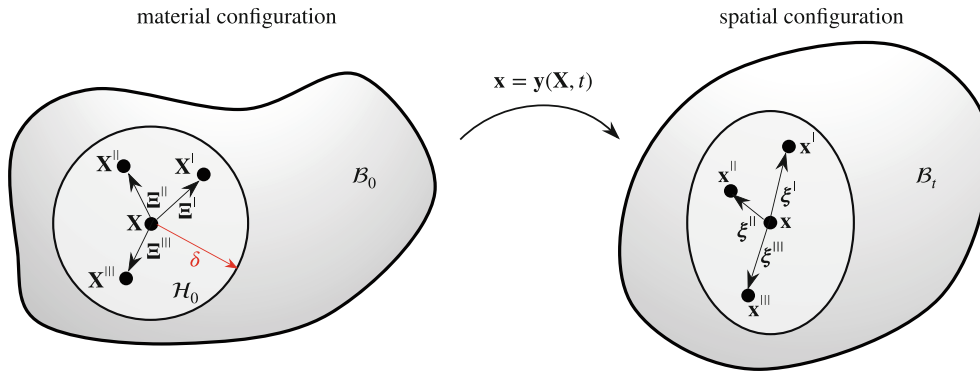
FIGURE 1 Illustration of a continuum body $\mathcal{B}_0$ in the material configuration (left) and its spatial counterpart $\mathcal{B}_t$ (right). In CPD, a point $\mathbf{X}$ interacts with sets of neighbors $\{\mathbf{X}^{\mathsf{I}}, \mathbf{X}^{\mathsf{II}}, \mathbf{X}^{\mathsf{III}}\}$ in a finite neighborhood $\mathcal{H}_0$ defined by the horizon size δ

2 | CONTINUUM-KINEMATICS-INSPIRED PERIDYNAMICS

We adopt continuum-kinematics-inspired peridynamics (CPD). This section lays down its fundamentals including the kinematics, the governing equations, and the employed constitutive law.

2.1 | Kinematics

Figure 1 depicts a continuous body occupying the material configuration $\mathcal{B}_0 \subset \mathbb{R}^3$ at time $t = 0$. It is transformed into the spatial configuration $\mathcal{B}_t \subset \mathbb{R}^3$ via the nonlinear deformation map $\mathbf{y}$ as $\mathbf{x} = \mathbf{y}(\mathbf{X}, t) : \mathcal{B}_0 \times \mathbb{R}_+ \to \mathcal{B}_t$. A continuum point is described by its position vector $\mathbf{X}$ in the undeformed configuration and its spatial counterpart $\mathbf{x}$. The main idea of PD is to measure the interactions of a point and its neighboring points within a finite distance. This neighborhood is commonly referred to as the peridynamic horizon $\mathcal{H}_0(\mathbf{X}) \subset \mathcal{B}_0$ and is characterized by the horizon size δ. Employing a Lagrangian perspective, δ is commonly the radius of a sphere in the material configuration. CPD in particular considers a whole set of neighbors

$$\{\mathbf{X}^{\mathsf{I}}, \mathbf{X}^{\mathsf{II}}, \mathbf{X}^{\mathsf{III}}\} \quad \forall \quad \mathbf{X}^{\mathsf{I}} \in \mathcal{H}_0(\mathbf{X}), \quad \mathbf{X}^{\mathsf{II}} \in \mathcal{H}_0(\mathbf{X}), \quad \mathbf{X}^{\mathsf{III}} \in \mathcal{H}_0(\mathbf{X}), \tag{1}$$

and their spatial counterparts $\{\mathbf{x}^{\mathsf{I}}, \mathbf{x}^{\mathsf{II}}, \mathbf{x}^{\mathsf{III}}\}$. The corresponding relative position vectors in the initial and the current configuration, respectively, are given by

$$\mathbf{\Xi}^{\mathsf{I}} = \mathbf{X}^{\mathsf{I}} - \mathbf{X} \quad \text{and} \quad \boldsymbol{\xi}^{\mathsf{I}} = \mathbf{x}^{\mathsf{I}} - \mathbf{x} = \mathbf{y}(\mathbf{X}^{\mathsf{I}}) - \mathbf{y}(\mathbf{X}), \tag{2}$$

$$\mathbf{\Xi}^{\mathsf{II}} = \mathbf{X}^{\mathsf{II}} - \mathbf{X} \quad \text{and} \quad \boldsymbol{\xi}^{\mathsf{II}} = \mathbf{x}^{\mathsf{II}} - \mathbf{x} = \mathbf{y}(\mathbf{X}^{\mathsf{II}}) - \mathbf{y}(\mathbf{X}), \tag{3}$$

$$\mathbf{\Xi}^{\mathsf{III}} = \mathbf{X}^{\mathsf{III}} - \mathbf{X} \quad \text{and} \quad \boldsymbol{\xi}^{\mathsf{III}} = \mathbf{x}^{\mathsf{III}} - \mathbf{x} = \mathbf{y}(\mathbf{X}^{\mathsf{III}}) - \mathbf{y}(\mathbf{X}). \tag{4}$$

The theory of CPD owes its name to the representation of the kinematics that is inspired by the basic elements of classical continuum kinematics. To accurately capture the key features of a deformation, viable measures are introduced that correspond to line, area, and volume elements in the spatial configuration. In CPD, the first relative deformation measure is $\boldsymbol{\xi}^{\mathsf{I}} = \mathbf{x}^{\mathsf{I}} - \mathbf{x}$, as introduced above, which serves as a descriptor of the change of length, in spirit analogous to the deformation gradient $\mathbf{F} := \text{Grad}\, \mathbf{y}$ in CCM. The change of area is captured by the second relative deformation measure $\boldsymbol{a}^{\mathsf{I/II}} = \boldsymbol{\xi}^{\mathsf{I}} \times \boldsymbol{\xi}^{\mathsf{II}}$, which is related to the cofactor $\mathbf{K} := \text{Cof}\, \mathbf{F}$ in Nanson's formula. Reminiscent of the Jacobian $J := \text{Det}\, \mathbf{F}$, the third relative deformation measure $v^{\mathsf{I/II/III}} = [\boldsymbol{\xi}^{\mathsf{I}} \times \boldsymbol{\xi}^{\mathsf{II}}] \cdot \boldsymbol{\xi}^{\mathsf{III}}$ is associated with volume. An overview of the kinematic measures in CCM and CPD is given in Table 1. In the limit of $\delta \to 0$ the nonlocal kinematic measures can cover the local ones. Consequently, the nonlocal kinematics of CPD are geometrically exact. At the same time, they allow us not only to consider one-neighbor interactions associated to classical bond-based PD, but also two-neighbor interactions and three-neighbor interactions are accounted for.

TABLE 1 Local kinematic measures versus nonlocal kinematic measures of CPD

	Relative length measure	Relative area measure	Relative volume measure
CCM	Deformation gradient $\mathbf{F}$	Cofactor $\mathbf{K}$	Determinant J
	$\mathbf{F} := \mathrm{Grad}\,\mathbf{y}$	$\mathbf{K} := \mathrm{Cof}\,\mathbf{F}$	$J := \mathrm{Det}\,\mathbf{F}$
CPD	$\xi = \mathbf{x}^{\mathsf{I}} - \mathbf{x}$	$\boldsymbol{a}^{\mathsf{I/II}} = \xi^{\mathsf{I}} \times \xi^{\mathsf{II}}$	$v^{\mathsf{I/II/III}} = [\xi^{\mathsf{I}} \times \xi^{\mathsf{II}}] \cdot \xi^{\mathsf{III}}$
	One-neighbor interactions	Two-neighbor interactions	Three-neighbor interactions

2.2 | Balance equations

The motion of a body is governed by the balance of linear momentum. Here, we consider the quasi-static case which states that the sum of the internal force density per volume $\mathbf{b}_0^{\mathrm{int}}$ and the external force density per volume $\mathbf{b}_0^{\mathrm{ext}}$ vanishes, that is

$$\mathbf{b}_0^{\mathrm{int}} + \mathbf{b}_0^{\mathrm{ext}} = \mathbf{0} \quad \Rightarrow \quad \int_{\mathcal{H}_0} \mathbf{p}^{\mathsf{I}}\, \mathrm{d}V^{\mathsf{I}} + \mathbf{b}_0^{\mathrm{ext}} = \mathbf{0}\ . \tag{5}$$

Based on the nonlocal nature of peridynamics, summing up the interaction forces of a point via integrating the force density per volume squared $\mathbf{p}^{\mathsf{I}}$ over the horizon renders the internal force density per volume. The set of balance equations that is required to describe the system is completed by the balance of angular momentum

$$\int_{\mathcal{H}_0} \xi^{\mathsf{I}} \times \mathbf{p}^{\mathsf{I}}\, \mathrm{d}V^{\mathsf{I}} = \mathbf{0}\ . \tag{6}$$

The force density $\mathbf{p}^{\mathsf{I}}$ can be split into terms corresponding to one-, two-, and three-neighbor interactions, as will be elaborated in the subsequent section. A detailed discussion of the thermodynamic foundation of CPD is provided by Javili et al.[16]

2.3 | Constitutive law

The starting point of deriving a constitutive law for hyperelastic material behavior is the point-wise stored energy density given by

$$\psi = \int_{\mathcal{H}_0} \frac{1}{2}\psi_1^{\mathsf{I}}\, \mathrm{d}V^{\mathsf{I}} + \int_{\mathcal{H}_0} \int_{\mathcal{H}_0} \frac{1}{3}\psi_2^{\mathsf{I/II}}\, \mathrm{d}V^{\mathsf{II}}\mathrm{d}V^{\mathsf{I}} + \int_{\mathcal{H}_0} \int_{\mathcal{H}_0} \int_{\mathcal{H}_0} \frac{1}{4}\psi_3^{\mathsf{I/II/III}}\, \mathrm{d}V^{\mathsf{III}}\mathrm{d}V^{\mathsf{II}}\mathrm{d}V^{\mathsf{I}}\ , \tag{7}$$

where $\psi_1^{\mathsf{I}}, \psi_2^{\mathsf{I/II}}$, and $\psi_3^{\mathsf{I/II/III}}$ denote the contributions from one-, two-, and three-neighbor interactions, respectively. The coefficients one-half, one-third, and one-fourth are introduced to avoid double, triple, and quadruple counting, respectively, since the multiple integrals lead to considering every point multiple times. If the terms are expressed with respect to the scalar-valued line, area, and volume measures l, a, and v, the balance of angular momentum is fulfilled a priori, see Javili et al.[16] These measures are given by

$$l := |\xi^{\mathsf{I}}|, \quad a := |\boldsymbol{a}^{\mathsf{I/II}}|, \quad v := |v^{\mathsf{I/II/III}}|\ , \tag{8}$$

with their material counterparts

$$L := |\Xi^{\mathsf{I}}|, \quad A := |\mathbf{A}^{\mathsf{I/II}}|, \quad V := |V^{\mathsf{I/II/III}}|\ . \tag{9}$$

In an intuitive manner, here, each energy contribution is described by a harmonic potential as follows

$$\psi_1^{\mathsf{I}} = \frac{1}{2}C_1 L\left[\frac{l}{L} - 1\right]^2, \quad \psi_2^{\mathsf{I/II}} = \frac{1}{2}C_2 A\left[\frac{a}{A} - 1\right]^2, \quad \psi_3^{\mathsf{I/II/III}} = \frac{1}{2}C_3 V\left[\frac{v}{V} - 1\right]^2. \tag{10}$$

In this fashion, the material constants of CPD, that is, C_1, C_2, and C_3, can be immediately interpreted as the resistance against the change of length of a bond between two points, the resistance against the change of area spanned by three points and the resistance against the change of volume formed by four points, respectively. Note that three parameters are necessary to describe isotropic elastic material behavior at finite deformations. This is similar to nonlinear CCM, which shall be compared with CPD since CPD is inherently formulated for large deformations. The number of material parameters for isotropic linear elasticity in CCM reduces to two due to the small deformations assumption, which of course can also be imposed on CPD.[18]

With the expression for the energy densities at hand, a constitutive law can be established. In doing so, the force density is divided into three parts associated with the three types of interactions, that is

$$\mathbf{p}^| = \mathbf{p}_1^| + \mathbf{p}_2^| + \mathbf{p}_3^| . \tag{11}$$

From the dissipation inequality and via a Coleman-Noll-like procedure for elasticity it eventually follows

$$\mathbf{p}_1^| = \frac{\partial \psi_1^|}{\partial \xi^|} = C_1 \left[\frac{l}{L} - 1 \right] \frac{\xi^|}{|\xi^||} , \tag{12}$$

$$\mathbf{p}_2^| = \int_{\mathcal{H}_0} 2\xi^{||} \times \frac{\partial \psi_2^{|/||}}{\partial \mathbf{a}^{|/||}} \, dV^{||} = \int_{\mathcal{H}_0} 2\xi^{||} \times C_2 \left[\frac{a}{A} - 1 \right] \frac{\mathbf{a}^{|/||}}{|\mathbf{a}^{|/||}|} dV^{||} , \tag{13}$$

$$\mathbf{p}_3^| = \int_{\mathcal{H}_0} \int_{\mathcal{H}_0} 3\xi^{||} \times \xi^{|||} \frac{\partial \psi_3^{|/||/|||}}{\partial v^{|/||/|||}} \, dV^{|||} dV^{||} = \int_{\mathcal{H}_0} \int_{\mathcal{H}_0} 3\xi^{||} \times \xi^{|||} C_3 \left[\frac{v}{V} - 1 \right] \frac{v^{|/||/|||}}{|v^{|/||/|||}|} \, dV^{|||} dV^{||} . \tag{14}$$

3 | KINEMATICALLY COUPLED NONLOCAL INTERFACE

In the following section, we introduce an approach on how to treat nonlocal material interfaces via a kinematic coupling. The main concept is presented in Section 3.1, while Section 3.2 gives details about the computational implementation.

3.1 | Concept

We consider a heterogeneous body that occupies the domain $\mathcal{B}_0$ in the material configuration. As it is depicted in Figure 2 for a two-dimensional problem (for illustration), the body is composed of two homogeneous constituents. That is
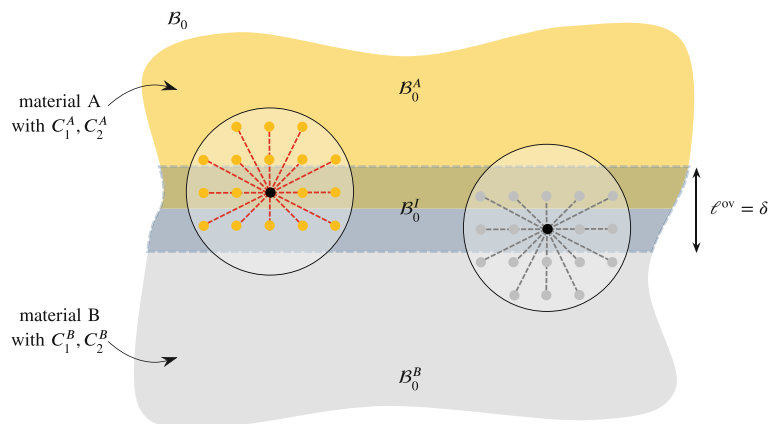
FIGURE 2 A heterogeneous body is composed of material A and material B, occupying the subdomains $\mathcal{B}_0^A$ and $\mathcal{B}_0^B$, respectively. A point directly interacts only with neighbors of the same material. However, the materials are kinematically coupled in an extended interfacial region, that is, the overlap domain $\mathcal{B}_0^I = \mathcal{B}_0^A \cap \mathcal{B}_0^B$. A two-dimensional illustration is given for the sake of illustration

material A, defined by the material constants C_1^A and C_2^A, in the subdomain $\mathcal{B}_0^A$ and material B, with C_1^B and C_2^B, occupying the subdomain $\mathcal{B}_0^B$. According to local continuum mechanics, the material interface between the two components is a distinct sharp line. In this contribution, we propose that in CPD, the two constituents are connected by an interfacial region of finite thickness. This extended nonlocal interface spans the subdomain $\mathcal{B}_0^I$, where the two material domains overlap, that is, $\mathcal{B}_0^I = \mathcal{B}_0^A \cap \mathcal{B}_0^B$. Within this region, the materials are perfectly bonded via a purely geometrical constraint. This is realized through pairs of peridynamic points of different materials sharing the same degree of freedom (DOF) and thus displacing equally. Conceptually speaking, the pairs are connected via infinitely stiff springs. The coupling is purely kinematic in the sense that the calculation of the interaction forces is carried out only within the single homogeneous materials. Hence, it can be described as a Dirichlet-type coupling with decoupled force computations. The nonlocal interface of finite thickness is reminiscent of an interphase that shows a slightly deviating behavior compared to the primary components, although no additional set of material parameters is assigned. Since the horizon size δ describes the degree of nonlocality of peridynamics, it seems reasonable to choose this parameter as the size of the overlap zone[*], which is denoted as ℓ^{ov} and which refers to the dimension perpendicular to the interface. Consequently, in the limit of a vanishing horizon, that is, $\delta \to 0$, a sharp interface is recovered. The concept of an overlap region of $\ell^{\text{ov}} = \delta$ can be compared to the application of boundary conditions in PD. To ensure a sufficient spread of the prescribed deformation into the bulk material, it is customary to apply the boundary conditions to additional material layers of depth δ along the boundaries of the actual geometry. This is true also for a material interface where the deformation of one material component needs to be adequately passed on to the other.

As in the presented interface approach interactions are computed only within a homogeneous material, the use of the material parameters is straightforward and does not involve mixture rules. Since peridynamic material parameters describe the properties of an interaction between points, rather than the properties of a point itself, interactions between points of different materials are not characterized explicitly. If only one-neighbor interactions are present, different kinds of mixture rules can be implemented to determine the property of a bond across the interface.[29] For multi-neighbor interactions, however, the behavior is additionally characterized by the ratio of the material parameters. For instance, in two dimensions, Poisson-like effects are described by the ratio C_2/C_1. This ratio is not unique if different material points are parts of the interaction and thus, mixture rules are no longer applicable.

Moreover, conceptually, an interface does not necessarily imply one- or multi-neighbor interactions between the two constituents. Depending on the types of materials and how they are joined, neither fiber connections nor chemical bonds might exist across the interface. The bonding might be predominantly mechanical in nature. In these cases, a purely kinematic contact is suitable. Also, note that we consider peridynamic bonds that fundamentally differ from bonds in MD, which motivates an alternative methodology.

3.2 | Computational implementation

The domains $\mathcal{B}_0^A$ and $\mathcal{B}_0^B$ are discretized into a grid of peridynamic points $\mathcal{P}^a$ and $\mathcal{P}^b$ identified by $\mathbb{X}^a$ and $\mathbb{X}^b$, respectively, with coinciding discretizations in the overlap region $\mathcal{B}_0^I$. The equation to solve is the nonlocal balance of linear momentum (5), whose left-hand side is referred to as the residual vector $\mathbf{R}$ and its discretized counterpart $\mathbb{R}$. In the sense of collocation, the balance of linear momentum is evaluated at each grid point and the global residual vector is constructed from the point-wise contributions. In this work, the point-wise discretized residual vector is stated in a general form $\mathbb{R}^\bullet$ for a point $\mathcal{P}^\bullet$ with $\{\bullet\} = \{a, b\}$ to stress the use of differing material parameters for $\mathcal{P}^a$ and $\mathcal{P}^b$. It can be written as

$$\mathbb{R}^\bullet = \mathbb{R}_1^\bullet + \mathbb{R}_2^\bullet + \mathbb{R}_3^\bullet, \tag{15}$$

with the contributions resulting from one-, two-, and three-neighbor interactions, respectively, as follows

$$\mathbb{R}_1^\bullet = \sum_{\substack{i=1 \\ i \neq \bullet}}^{\#\mathcal{N}} C_1^\bullet \left[\frac{1}{|\Xi^i|} - \frac{1}{|\xi^i|} \right] \xi^i V_1, \tag{16}$$

---

[*]The feasibility of this assumption and the significance of the overlap size is shortly assessed through numerical examples in Section 4.3.

$$\mathbb{R}_2^\bullet = \sum_{\substack{i=1\\i\neq\bullet}}^{\#\mathcal{N}} \sum_{\substack{j=1\\j\neq i\\j\neq\bullet}}^{\#\mathcal{N}} 2C_2^\bullet \left[\frac{1}{|\Xi^{\mathrm{I}} \times \Xi^{\mathrm{II}}|} - \frac{1}{|\xi^{\mathrm{I}} \times \xi^{\mathrm{II}}|} \right] \left[[\xi^{\mathrm{II}} \cdot \xi^{\mathrm{II}}]\xi^{\mathrm{I}} - [\xi^{\mathrm{I}} \cdot \xi^{\mathrm{II}}]\xi^{\mathrm{II}} \right] V_2 \,, \tag{17}$$

$$\mathbb{R}_3^\bullet = \sum_{\substack{i=1\\i\neq\bullet}}^{\#\mathcal{N}} \sum_{\substack{j=1\\j\neq i\\j\neq\bullet}}^{\#\mathcal{N}} \sum_{\substack{k=1\\k\neq j\\k\neq i\\k\neq\bullet}}^{\#\mathcal{N}} 3C_3^\bullet[\xi^{\mathrm{II}} \times \xi^{\mathrm{III}}] \left[\frac{1}{|\left[\Xi^{\mathrm{I}} \times \Xi^{\mathrm{II}}\right] \cdot \Xi^{\mathrm{III}}|} - \frac{1}{|\left[\xi^{\mathrm{I}} \times \xi^{\mathrm{II}}\right] \cdot \xi^{\mathrm{III}}|} \right] \left[[\xi^{\mathrm{I}} \times \xi^{\mathrm{II}}] \cdot \xi^{\mathrm{III}} \right] V_3 \,, \tag{18}$$

for a set of neighbors $\{i, j, k\}$. Here, V_1, V_2, and V_3 refer to the volume fractions of the horizon that are associated with the respective interaction. The process of constructing the global residual vector of size #DOFs from the individual contributions is called assembly. Hence, we introduce the CPD assembly operator $\mathbf{A}$. The operator ensures that the point-wise contributions are assigned to the correct global entries according to the DOFs of the individual points. The assembly procedure reads

$$\mathbb{R} = \mathop{\mathbf{A}}_{\forall \mathcal{P}^\bullet} \mathbb{R}^\bullet = \mathop{\mathbf{A}}_{\forall \mathcal{P}^\bullet} \left[\mathbb{R}_1^\bullet + \mathbb{R}_2^\bullet + \mathbb{R}_3^\bullet \right] \,. \tag{19}$$

In this fashion, the operator likewise takes care of the interface region. A pair of points $\mathcal{P}^a \in \mathcal{B}_0^I$ and $\mathcal{P}^b \in \mathcal{B}_0^I$ with coinciding position vectors $\mathbb{X}^a$ and $\mathbb{X}^b$ in the reference configuration share the DOFs and their contributions are assigned to the same entries by the assembly operator. Thus, in the overlap region, pairs of points of *dissimilar* material contribute to the *same* component of the global vector. The system of equations $\mathbb{R} = \mathbb{0}$ is solved for the global discretized deformation vector $\mathbb{x}$. Since the nonlinearity of the problem necessitates an iterative scheme, we apply the Newton–Raphson method. The method relies on a linearization of the system that results in calculating the tangent stiffness matrix $\mathbb{K}_k$ at every iteration k to approximate the residual $\mathbb{R}_{k+1}$ with

$$\mathbb{R}_{k+1} = \mathbb{R}_k + \left[\frac{\partial \mathbb{R}}{\partial \mathbb{x}} \right]_k \Delta \mathbb{x}_k = \mathbb{R}_k + \mathbb{K}_k \Delta \mathbb{x}_k \overset{!}{=} \mathbb{0} \,. \tag{20}$$

Subsequent to solving the linear system of equations given by

$$\Delta \mathbb{x}_k = - \left[\mathbb{K}_k \right]^{-1} \mathbb{R}_k \,, \tag{21}$$

the deformation vector is updated according to

$$\mathbb{x}_{k+1} = \mathbb{x}_k + \Delta \mathbb{x}_k \,. \tag{22}$$

The iterations terminate if the norm of the residual is within a given tolerance. For large deformations, the application of the load can be split up into N load steps. Analogous to the residual vector, the tangent stiffness matrix is first computed point-wise. Thereafter, the assembly operator is used to construct the global stiffness matrix. For the points $\mathcal{P}^a, \mathcal{P}^\alpha \in \mathcal{B}_0^A$ and the points $\mathcal{P}^b, \mathcal{P}^\beta \in \mathcal{B}_0^B$, respectively, with $\{\bullet\circ\} = \{a\alpha, b\beta\}$, the point-wise discretized stiffness matrix reads

$$\mathbb{K}^{\bullet\circ} = \mathbb{K}_1^{\bullet\circ} + \mathbb{K}_2^{\bullet\circ} + \mathbb{K}_3^{\bullet\circ} = \frac{\partial \mathbb{R}_1^\bullet}{\partial \mathbb{x}^\circ} + \frac{\partial \mathbb{R}_2^\bullet}{\partial \mathbb{x}^\circ} + \frac{\partial \mathbb{R}_3^\bullet}{\partial \mathbb{x}^\circ} \,, \tag{23}$$

with contributions from one-, two-, and three-neighbor interactions. The full expressions are given in Appendix A. The individual contributions are sorted into the global stiffness matrix according to their DOFs through the assembly procedure, that is,

$$\mathbb{K} = \mathop{\mathbf{A}}_{\forall \mathcal{P}^\bullet \mathcal{P}^\circ} \mathbb{K}^{\bullet\circ} = \mathop{\mathbf{A}}_{\forall \mathcal{P}^\bullet \mathcal{P}^\circ} \left[\mathbb{K}_1^{\bullet\circ} + \mathbb{K}_2^{\bullet\circ} + \mathbb{K}_3^{\bullet\circ} \right] \,. \tag{24}$$

This implies that, within the overlap region, an entry of the global tangent stiffness matrix is composed of contributions from points $\mathcal{P}^a$ and $\mathcal{P}^\alpha$ of material A as well as from points $\mathcal{P}^b$ and $\mathcal{P}^\beta$ of material B. Figure 3 depicts the sparsity pattern of an example stiffness matrix. The color code visualizes the overlap zone where the DOFs are shared by the two material domains. The general procedure for solving a three-dimensional deformation problem involving a material interface is sketched in a pseudo-code in Algorithm 1. All numerical examples in this work are carried out using MATLAB.
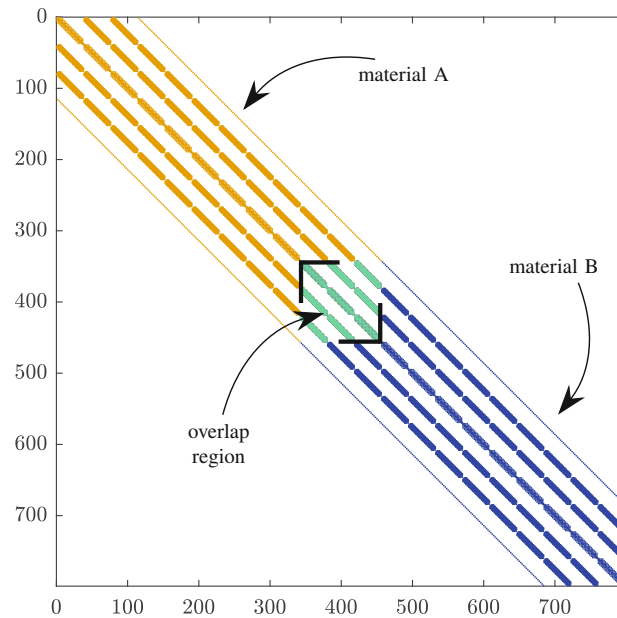
FIGURE 3 Sparsity pattern of an example global stiffness matrix (for 798 DOFs) composed of contributions from material A (yellow), material B (blue), and mixed contributions at shared DOFs in the overlap region (green)

Algorithm 1. Outline of solving the deformation problem in the presence of a nonlocal interface following the approach discussed above

- assign DOFs globally to $\mathcal{B}_0$
- neighbor search within $\mathcal{B}_0^A$: for every point $\mathcal{P}^a$ find neighboring points $\mathcal{P}^i \in \mathcal{B}_0^A$
- neighbor search within $\mathcal{B}_0^B$: for every point $\mathcal{P}^b$ find neighboring points $\mathcal{P}^i \in \mathcal{B}_0^B$

for load step $n \in N$ **do**
  • prescribe boundary conditions
  for iteration k **do**
    for $\mathcal{P}^a \in \mathcal{B}_0^A$ **do**
      • compute $\mathbb{R}_k^a$ using C_1^A, C_2^A, C_3^A and neighbors $\mathcal{P}^i, \mathcal{P}^j, \mathcal{P}^k \in \mathcal{B}_0^A$
      • assemble $\mathbb{R}_k^a$ into global $\mathbb{R}_k$ according to DOFs of $\mathcal{P}^a$
    end
    for $\mathcal{P}^b \in \mathcal{B}_0^B$ **do**
      • compute $\mathbb{R}_k^b$ using C_1^B, C_2^B, C_3^B and neighbors $\mathcal{P}^i, \mathcal{P}^j, \mathcal{P}^k \in \mathcal{B}_0^B$
      • assemble $\mathbb{R}_k^b$ into global $\mathbb{R}_k$ according to DOFs of $\mathcal{P}^b$
    end
    if global $|\mathbb{R}_k|>$tolerance **then**
      for $\mathcal{P}^a \in \mathcal{B}_0^A$ **do**
        • compute $\mathbb{K}_k^{a\alpha}$ using C_1^A, C_2^A, C_3^A and neighbors $\mathcal{P}^i, \mathcal{P}^j, \mathcal{P}^k \in \mathcal{B}_0^A$
        • assemble $\mathbb{K}_k^{a\alpha}$ into global $\mathbb{K}_k$ according to DOFs of $\mathcal{P}^a$ and $\mathcal{P}^\alpha$
      end
      for $\mathcal{P}^b \in \mathcal{B}_0^B$ **do**
        • compute $\mathbb{K}_k^{b\beta}$ using C_1^B, C_2^B, C_3^B and neighbors $\mathcal{P}^i, \mathcal{P}^j, \mathcal{P}^k \in \mathcal{B}_0^B$
        • assemble $\mathbb{K}_k^{b\beta}$ into global $\mathbb{K}_k$ according to DOFs of $\mathcal{P}^b$ and $\mathcal{P}^\beta$
      end
      • solve global linear system of equations $\Delta \mathbb{x}_k = - \left[\mathbb{K}_k \right]^{-1} \mathbb{R}_k$
      • update $\mathbb{x}_{k+1}^a$ and $\mathbb{x}_{k+1}^b$ for every $\mathcal{P}^a$ and $\mathcal{P}^b$ using $\Delta \mathbb{x}_k$
      • next iteration: $k \longleftarrow k + 1$
    end
  end
  • next load step: $n \longleftarrow n + 1$
end

4 | NUMERICAL STUDY OF BIMATERIAL INTERFACES

The aim of this section is to illustrate the proposed model through a collection of numerical examples. To this end, in Section 4.1, we carry out an extensive series of tests using different sets of material parameters, different loading conditions and different two-dimensional interface geometries. A convergence study for decreasing nonlocality, including a comparison to a local interface, is presented in Section 4.2. The influence of different sizes of the overlap region is investigated in Section 4.3, while Section 4.4 is concerned with a CPD interface at large deformations. In Section 4.5, we demonstrate the applicability of our approach to three-dimensional problems via a set of simulations.

4.1 | Two-dimensional examples

We investigate the nonlocal interface problem by means of a bimaterial unit square. The geometry is discretized into a peridynamic grid of points with grid spacing $\Delta = 0.01$. Following common practice in PD, we begin with a horizon size of $\delta = 3.01\Delta$ and extend the geometry by additional material layers of size δ at the edges where boundary conditions are to be imposed. In this way, a smooth application of the boundary conditions is ensured. Figure 4 depicts the three utilized load cases. In each case, we prescribe the displacement to the left and right boundary regions, that is, the outmost layer of the geometry as well as the additional material layers. The prescribed displacements result from imposing a uniform deformation gradient. Load case I refers to a uniaxial stretch in horizontal direction. In load case II, the boundary layers are expanded through a biaxial stretch. Shear in horizontal and vertical direction is applied to the boundary regions in load case III. In all cases, the sample is stretched or compressed, respectively, by 0.1 %. To begin with, small deformations as resulting from the loading are considered to ensure a meaningful comparison between parameters and energies with linear CCM. Large deformations are studied in Section 4.4. For each load case, we study three different types of interface geometries. The materials are either arranged left and right to each other (vertical interface), on top of each other (horizontal interface) or the interface runs at a 45° angle, always dividing the sample into equal halves. We refer to the left/bottom material as material A, in the following shown in blue, and the right/top one as material B, shown in red. The size of the overlap region is set to $\ell^{ov} = \delta$. Due to the two-dimensional nature of the problem, one- and two-neighbor interactions are active, while three-neighbor interactions are not present. Note that the primary parameters of CPD in a two-dimensional problem are C_1 and C_2. The level of compressibility of a material stems from the ratio of C_2 to C_1. Within this manuscript, we indicate compressibility in terms of the Poisson ratio ν to make it more intuitive for the reader. By comparing the CPD energy of a simple deformation state to that of a classical model, formulations for conversions of the material constants can be found. For an extensive derivation of the relationships between the material parameters of CPD and isotropic linear elasticity, see Ekiz et al.[22] For a two-dimensional problem the parameter conversion reads

$$\nu(C_1, C_2, \delta) = \frac{\frac{C_2}{C_1}\delta^3 + \frac{9}{64}}{\frac{C_2}{C_1}\delta^3 + \frac{27}{64}} \ . \tag{25}$$

Note that in the absence of C_2, that is, $C_2 = 0$, $\nu = 1/3$ is recovered in accordance with bond-based PD. We emphasize that here, ν is used for the sake of brevity but refers to the Poisson ratio ν_{2D} in two-dimensional problems, where $\nu_{2D} = 1$ is the two-dimensional incompressibility limit, achieved if $C_2/C_1 \to \infty$. It thus differs from its counterpart in three dimensions. The conversion reads $\nu_{3D} = \nu_{2D}/[1 + \nu_{2D}]$. To illustrate the presented interface approach for a variety of material parameters, three different sets of material constants are examined. Table 2 summarizes the utilized material parameters for all two-dimensional examples in this work. This section is concerned with Set $1 - 3$. The first set comprises materials of identical Poisson's ratios that differ in stiffness ($C_1^B = 100C_1^A$, $\nu^A = \nu^B = 0.1 \Rightarrow C_2^A(\delta = 0.0301) = -4 \times 10^3$, $C_2^B(\delta = 0.0301) = -4 \times 10^5$). Materials that are equally stiff but have different Poisson's ratios are considered in the second set ($C_1^A = C_1^B$, $\nu^A = 1/3 \Rightarrow C_2^A(\delta = 0.0301) = 0$, $\nu^B = 0.7 \Rightarrow C_2^B(\delta = 0.0301) = 1.9 \times 10^4$), whereas both stiffness and Poisson's ratio are varied in the third set ($C_1^A = 20C_1^B$, $\nu^A = 0.4 \Rightarrow \tilde{C}_2^A(\delta = 0.0301) = 1.7 \times 10^3$, $\nu^B = 0.2 \Rightarrow C_2^B(\delta = 0.0301) = -129$). Throughout this article, C_1^A is set to 1. In the remainder of this contribution, material constants are given in reference to Table 2 for the sake of brevity.

The simulation results of the three sets of material constants are assembled in Figures 5–7. The deformed configurations are depicted for the different load cases (columns) and the different material arrangements (rows). The figures
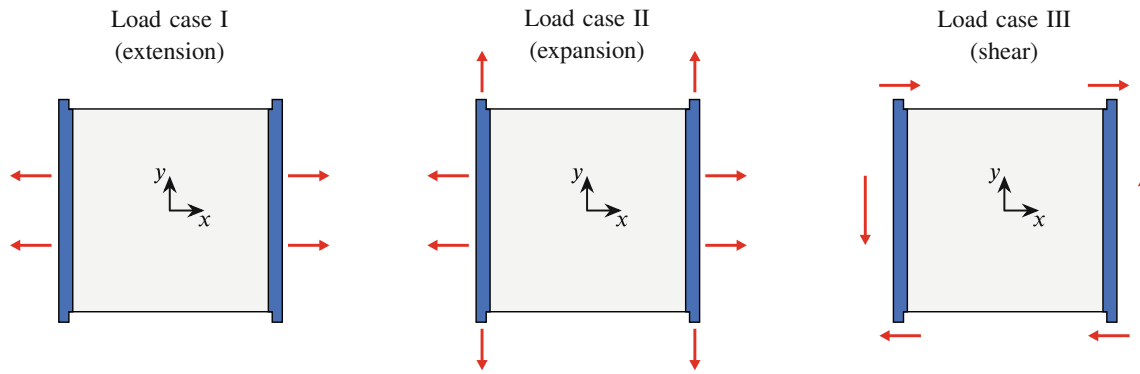
FIGURE 4 Three different load cases to study the applicability of the proposed model. The displacement is prescribed to the left and right boundary regions (colored in blue)

TABLE 2 Summary of the material parameters for all two-dimensional examples used in Sections 4.1–4.4

	SET 1	SET 2	SET 3	SET 4
C_1^B/C_1^A	100	1	1/20	1
$v^A(C_1^A, C_2^A, \delta)$	0.1	1/3	0.4	0.6
$C_2^A/C_1^A(v^A, \delta)$	$-\dfrac{7}{64}\dfrac{1}{\delta^3}$	0	$\dfrac{3}{64}\dfrac{1}{\delta^3}$	$\dfrac{9}{32}\dfrac{1}{\delta^3}$
$v^B(C_1^B, C_2^B, \delta)$	0.1	0.7	0.2	0.6
$C_2^B/C_1^B(v^B, \delta)$	$-\dfrac{7}{64}\dfrac{1}{\delta^3}$	$\dfrac{33}{64}\dfrac{1}{\delta^3}$	$-\dfrac{9}{128}\dfrac{1}{\delta^3}$	$\dfrac{9}{32}\dfrac{1}{\delta^3}$

Note: For an intuitive interpretation, the Poisson ratio v (under plane strain conditions) is indicated, which is converted to C_2/C_1 in CPD. The conversion is given in terms of δ as the horizon size varies throughout this article. C_1^A is always set to 1.

demonstrate the capability of our approach to handle different types of bimaterial interface problems. Throughout the test series, we observe that the behavior of the overlap region tends to adopt the behavior of the stiffer constituent. The high influence of the stiffer material is expected since its contributions to the shared DOFs are larger than those of the more compliant material. In general, the plots show that the kinematic coupling within the interfacial region results in a smooth transition between the dissimilar materials. What is particular about the example in Figure 6 is that $v^A = 1/3$ implies that material A is described solely by one-neighbor interactions. In the case of $v = 1/3$ in two-dimensional problems, CPD boils down to bond-based PD and two-neighbor interactions are not present. With our approach, a material with only one-neighbor interactions can easily be connected to a material with both one- and two-neighbor interactions.

Lastly, we point out that the plots illustrate how different levels of compressibility can easily be modeled with CPD. This can be observed especially for load case I (extension), where the amount of lateral contraction differs significantly throughout the tests depending on the material parameters. Since two-neighbor interactions define the resistance against the change of area, increasing C_2/C_1, which is associated with increasing v, leads to a stronger lateral contraction. This feature of CPD contributes to setting the stage for its wide use.

4.2 ┃ Nonlocality study and comparison to local interfaces

This section is concerned with a nonlocality study to analyze the influence of the horizon size on the material behavior especially at the interface. Figure 8 schematically depicts the general procedure. That is, the horizon size δ is decreased while the ratio of the horizon size to grid spacing δ/Δ is maintained. In PD literature, this approach is commonly referred to as δ-convergence[44,45] and employed to study the influence of nonlocal effects and the convergence towards the local solution. In this study, we set $\delta/\Delta = 8.01$ for increased numerical accuracy. For the sake of comparing the CPD results to CCM results, we carry out simulations using the finite element method (FEM). There, we adopt a linear elastic material
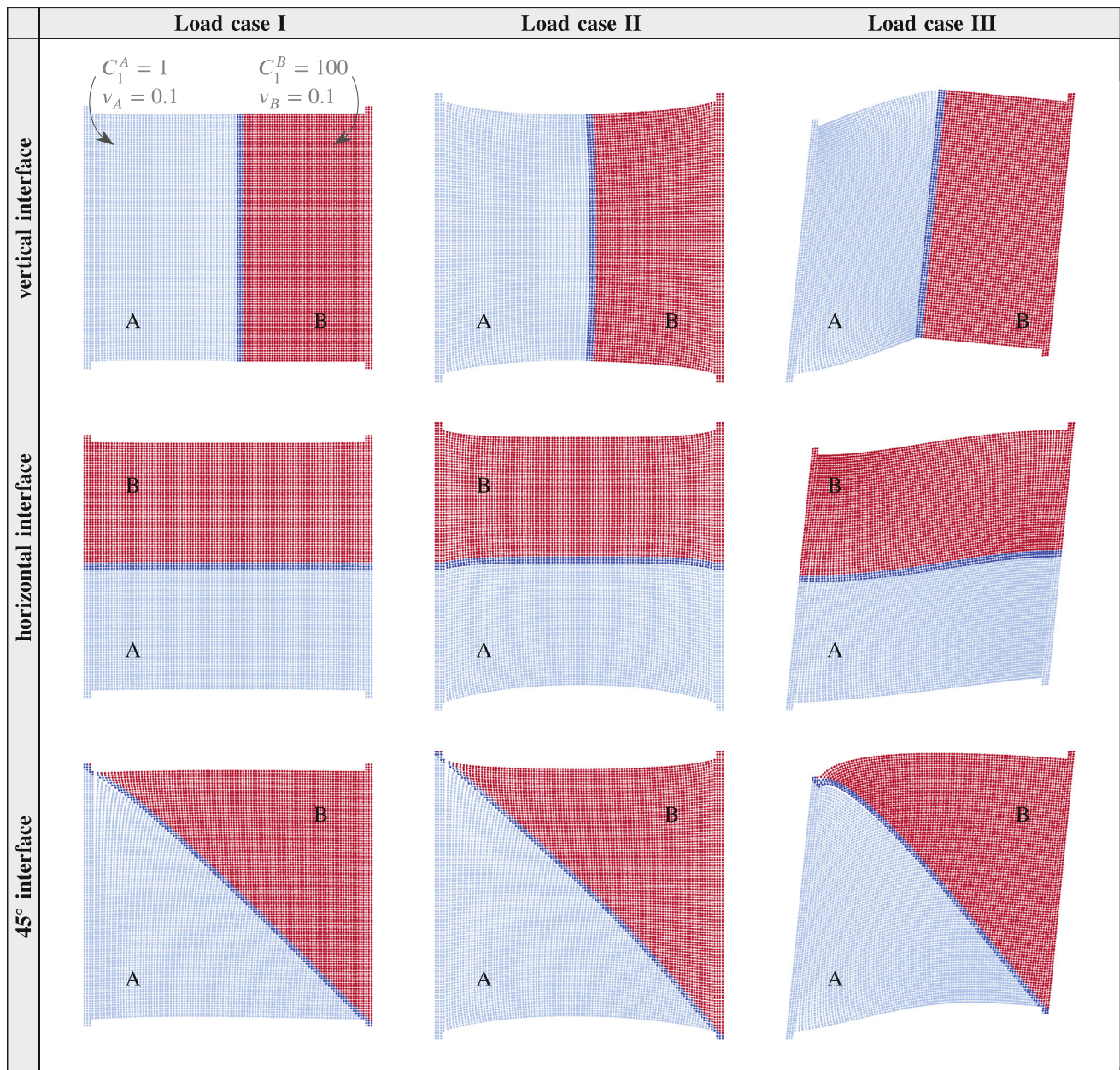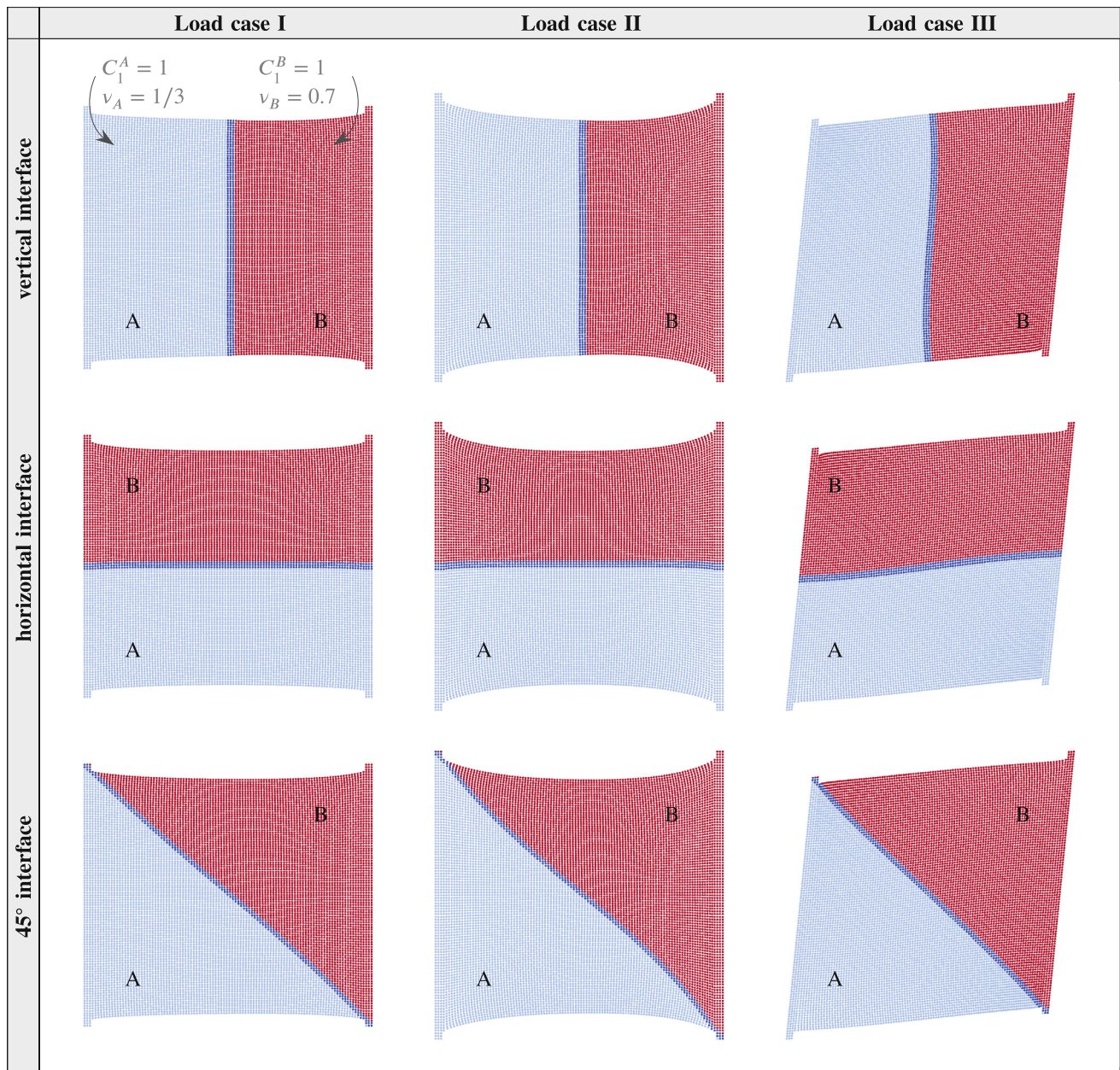
FIGURE 5 Deformed configurations of a unit square comprising material A (blue) and material B (red) that are equal in Poisson's ratio but differ in stiffness (parameter set 1 of Table 2). The deformation is magnified for the sake of visualization

model as it adequately compares to our CPD model within the small-strain regime. Our used FEM meshes are sufficiently fine. Due to surface effects, that is, differing behavior of points at the edges that do not have a full horizon, and unavoidable numerical inaccuracies, the resulting compressible behavior of the CPD sample slightly deviates from the prescribed value of ν. For an accurate comparison, we approximate ν from the geometry changes of the CPD domain to obtain a suitable value for the FEM simulation.

In the following, the results of the nonlocality study are illustrated for two example tests from Section 4.1 and one additional example that includes an interface between two identical materials. Figure 9 (top) corresponds to a test case with the first set of material parameters (see Table 2) and a horizontal interface loaded according to load case III. We plot the horizontal displacement along a vertical line of the specimen, as indicated in the figure. Here, two effects result from decreasing δ. First, the model tends to be more local and thus, nonlocal effects diminish in general. Second, the overlap region shrinks since its size equals the horizon size. As a result of these two effects, the nonlocal solutions converge to the
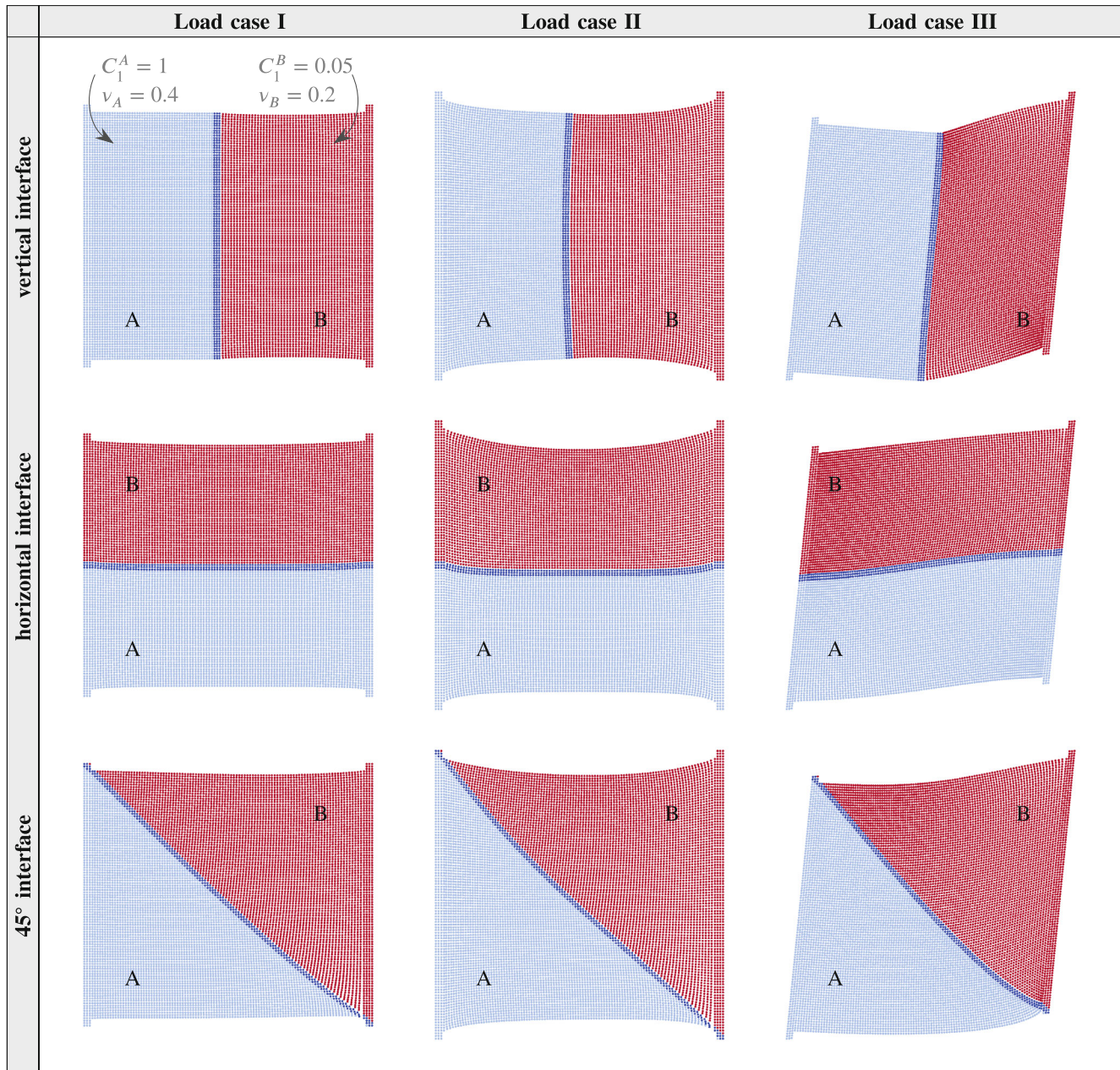
FIGURE 6 Deformed configurations of a unit square comprising material A (blue) and material B (red) that are equal in stiffness but differ in Poisson's ratio (parameter set 2 of Table 2). The deformation is magnified for the sake of visualization

local solution. Furthermore, the diagram shows that the points in the overlap region take on the behavior of the stiffer material, analogous to the observations in Section 4.1. In Figure 9 (center), the same conclusions can be drawn for the third set of material parameters (see Table 2) with a vertical interface subject to load case I. Again, the FEM solution including the sharp interface is approached with decreasing nonlocality of the CPD model. The last example is shown in Figure 9 (bottom). This example is included to analyze the proposed approach with regard to two identical materials (fourth parameter set, see Table 2) connected by an interface. Here, the geometry is extended by a hole in the center with a side length of 0.4. We apply load case I to a vertical interface. Moreover, we repeat the test with a homogeneous CPD material without interface for the sake of comparison. It can be seen in the diagram that the presence of the interface leads to slightly deviating displacements in the proximity of the interface. Due to the contact in the overlap region, the model "feels" the interface and the sample composed of two constituents can be distinguished from the homogeneous one. Nonetheless, the differences reduce with decreasing horizon size as expected and convergence towards the FEM

FIGURE 7   Deformed configurations of a unit square comprising material A (blue) and material B (red) that differ in stiffness and in Poisson's ratio (parameter set 3 of Table 2). The deformation is magnified for the sake of visualization

solution is obtained. Overall, the results consistently and coherently show that a local interface is recovered in the local limit of the nonlocal CPD model.

4.3 | Size of the overlap region

In Section 3.1, the size of the overlap region ℓ^{ov} was defined as the horizon size δ. However, the overlap size is not a strictly fixed parameter, but a flexible one. For example, choosing multiples of the horizon size is also conceivable. This motivates us to include an investigation of different overlap sizes in this section. We once more study the unit square with a horizontal interface and apply load case II. The third material parameter set is employed (see Table 2). For a constant horizon size of $\delta = 0.0501$ and $\delta/\Delta = 5.01$, we vary the overlap size ℓ^{ov} ($2\delta, \delta, \delta/2, \delta/4$). Figure 10 illustrates the resulting
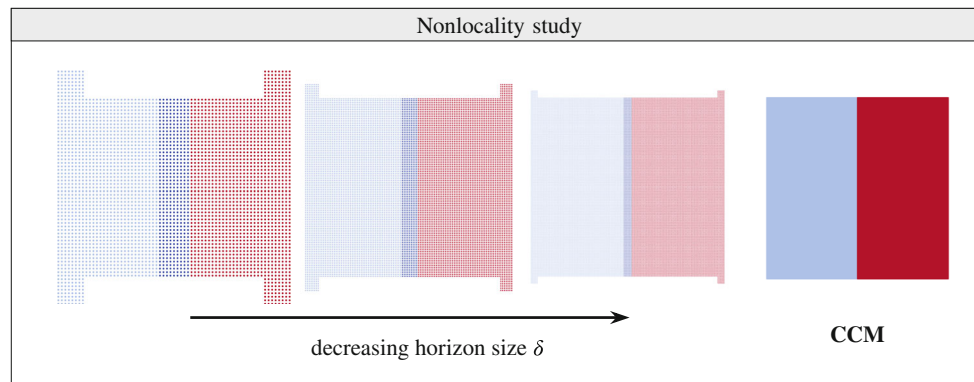
FIGURE 8 General procedure of a nonlocality study. The nonlocality parameter δ is decreased to approach a CCM model. The ratio of horizon size to grid spacing δ/Δ is kept constant

deformed configurations. The horizontal displacement along $X = 0.1$ is included in Figure 11 in comparison to the local solution resulting from a FEM simulation. As expected, the deformation differs mainly in the proximity of the interface. Since the bottom material is stiffer than the top material, the deformation of the interfacial layers is more similar to that of the bottom material. A small jump in displacement can be observed at the transition from the overlap region to the top material. With decreasing size of the overlap, the jump moves closer to the position of the sharp local interface at position $Y = 0$. Note that we do not expect convergence towards the local solution for decreasing overlap sizes as the horizon size is fixed at a nonlocal level. The results suggest that a flexible choice of the overlap size is possible. However, two aspects should be kept in mind. First, a choice of 2δ leads to a relatively far-reaching influence of the interface extending into the whole domain. Second, in case of a small overlap size, depending on the grid spacing, the overlap region might be discretized only into very few numerical layers. The rightmost plot in Figure 10 shows the extreme case of only one interfacial layer. Here, the coupling is not sufficient for a smooth transition between the two materials, resulting in the large jump in displacement in Figure 11. This aspect can be avoided using a finer discretization. Overall, it can be claimed that the adaption of the overlap size is not ruled out. Nevertheless, setting it to the nonlocality parameter δ fits to the idea of a nonlocal interface. *We emphasize, if $\delta \to 0$ all these options coincide and converge to the local solution of the problem.*

4.4 | Example at finite deformations

As a geometrically exact reformulation of peridynamics, CPD is naturally suitable for problems at finite deformations. Thus, in this section, we study the applicability of the proposed CPD interface approach to a bimaterial interface undergoing large deformations. To this end, we revisit a set of two-dimensional examples from Section 4.1, that is, a unit square with a vertical, a horizontal and a 45° interface described by the second set of material parameters (see Table 2). We set $\delta = 0.0301 = 3.01\Delta$ and $\ell^{ov} = \delta$. The sample is subject to load case I. This time, however, large deformations are imposed, that is, the sample is extended by 100%. Figure 12 depicts the resulting deformed configurations visualized in terms of horizontal and vertical displacement, respectively. The effect of two-neighbor interactions on the resistance against the change of area, reflected by the differences in ν_A and ν_B, is clearly visible at large deformations. Moreover, the smooth transition at the interface due to the perfect bonding within the overlap region is maintained even at this level of stretch. A key characteristic of CPD is the implementation via a fully implicit scheme. The nonlinear system of equations is solved by an iterative Newton–Raphson algorithm and the full expressions of the tangent stiffness matrix can be derived analytically in a form ready for implementation. Employing this solution method is extremely advantageous in terms of convergence rate. Table 3 shows the convergence behavior of the vertical interface example at large deformations. For five load steps, the normalized L_2-norm of the global residual vector $\mathbb{R}_k$ is indicated for every iteration. The stop criterion is defined by a tolerance of $tol = 1e-11$. A quadratic convergence rate, a key feature of the Newton–Raphson scheme, is observed. The efficiency and robustness of the Newton algorithm, leading to converged solutions after only a few iterations, is maintained in the presence of an interface even for large deformations. This suggests that the proposed approach can be readily applied to problems involving finite deformations.

LAURIEN ET AL.
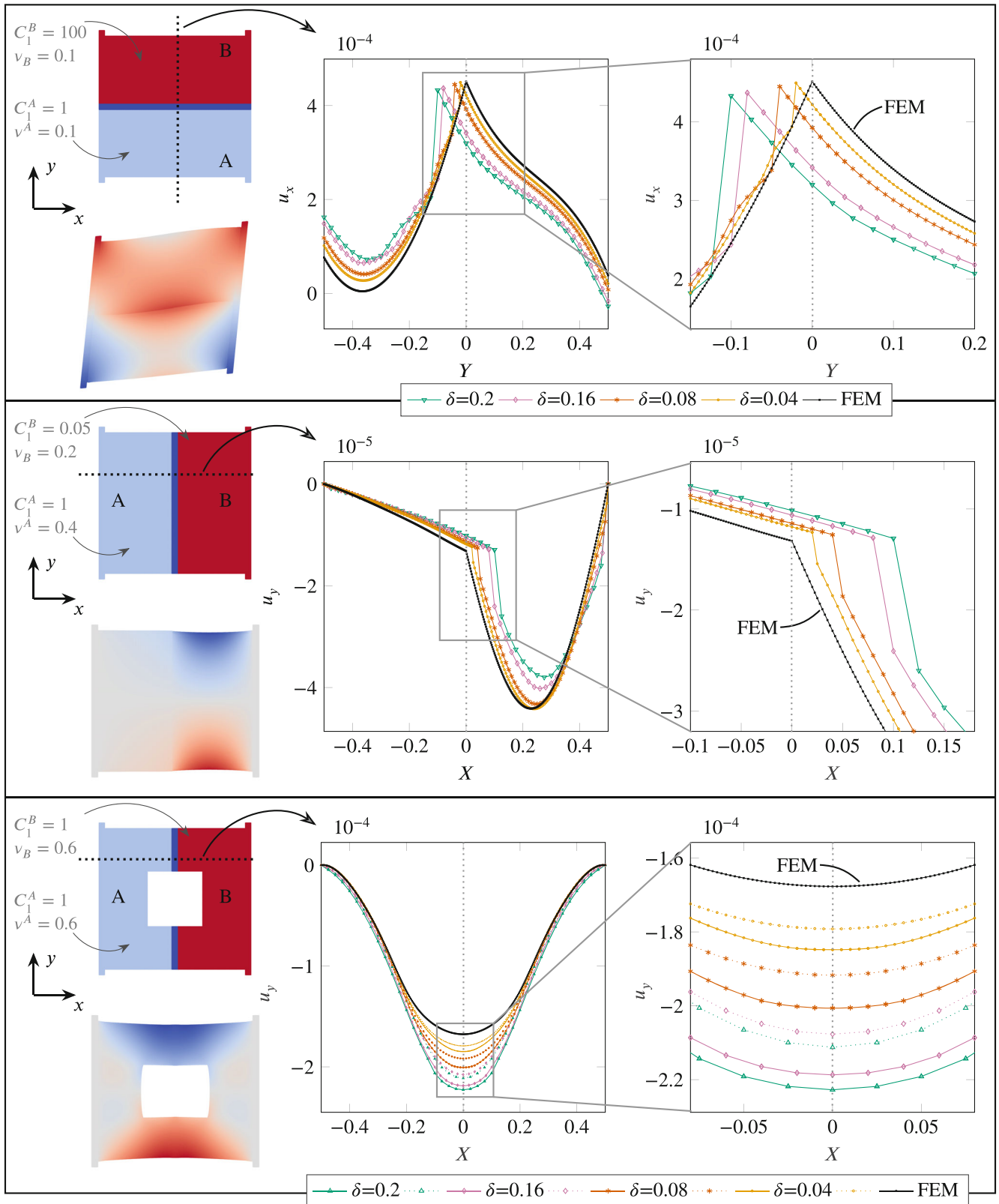
FIGURE 9 Illustration of the nonlocality study. Left: Undeformed and deformed sample (magnified deformation) resulting from a CPD simulation with material A (blue) and material B (red). Right: Plot of the displacement along the respective dotted lines and close-up of the proximity of the interface. Full lines correspond to a simulation with interface, dashed lines to a simulation with a homogeneous material
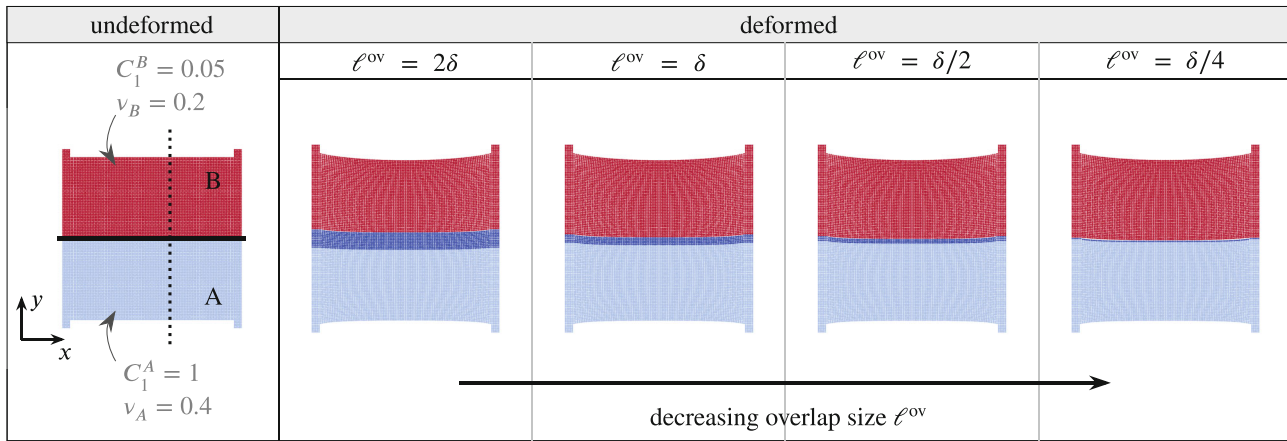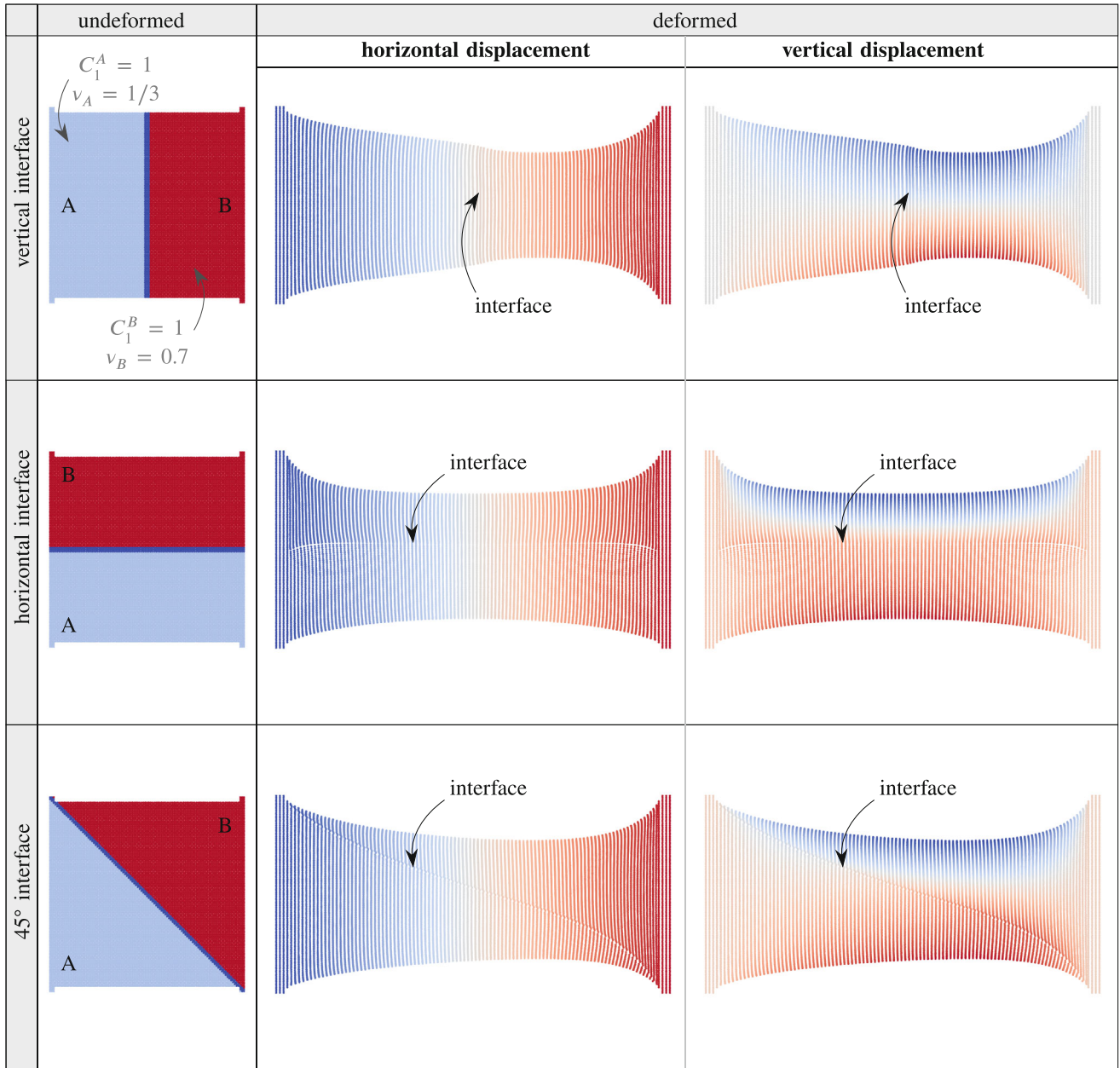
FIGURE 10 Magnified deformed configurations resulting from load case II and parameter set 3. Four different overlap sizes ℓ^{ov} are considered at a constant horizon size δ
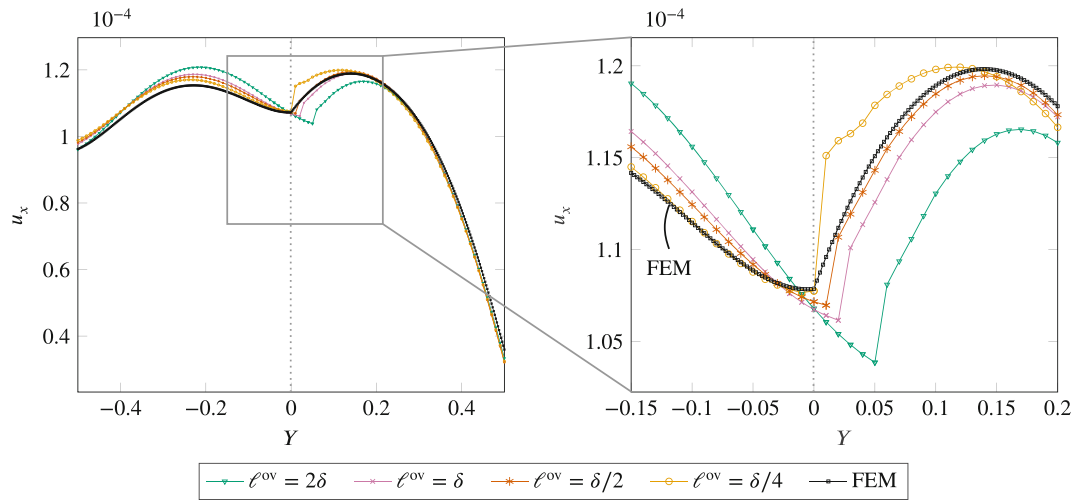
FIGURE 11 Horizontal displacement throughout the specimen for varying overlap sizes ℓ^{ov}. The right plot provides a close-up of the interface region. The large jump in displacement for $\ell^{ov} = \delta/4$ suggests that the overlap should not be much smaller than the horizon, as this contradicts the idea of a nonlocal interface

4.5 | Three-dimensional examples

This section aims at demonstrating the potential of our proposed model also for three-dimensional problems. We investigate two cuboids with a vertical and a horizontal interface, respectively, as depicted in their undeformed configurations in Figure 13 (first column). The horizon size is set to $\delta = 3.01\Delta$ with $\Delta = 0.035$. The load is applied analogously to the two-dimensional load cases presented in Section 4.1, again imposing small deformations of 0.1 % stretch and compression, respectively. In this three-dimensional simulation, we activate both one-neighbor and three-neighbor interactions. Accordingly, a large value of C_3/C_1 implies that the material is reluctant to volume changes, which can be converted to the classical Poisson ratio for three dimensions. The material parameters are given by $C_1^B = 20C_1^A$ and $v^A = 0.1 \Rightarrow C_3^A(\delta = 0.105) = -1.7 \times 10^6$ as well as $v^B = 0.4 \Rightarrow C_3^B(\delta = 0.105) = 1.4 \times 10^8$. We emphasize that, in contrast to the parameters in Table 2, we refer to three-dimensional parameters in this section. Figure 13 (second to fourth column) illustrates the respective deformed configurations. The results show that the proposed approach can easily handle also three-dimensional problems. The concept of a kinematic coupling can simply be adopted to a volumetric overlap region. Eventually, we point out that, importantly, the quadratic convergence of the Newton–Raphson algorithm is maintained for the three-dimensional model as well.
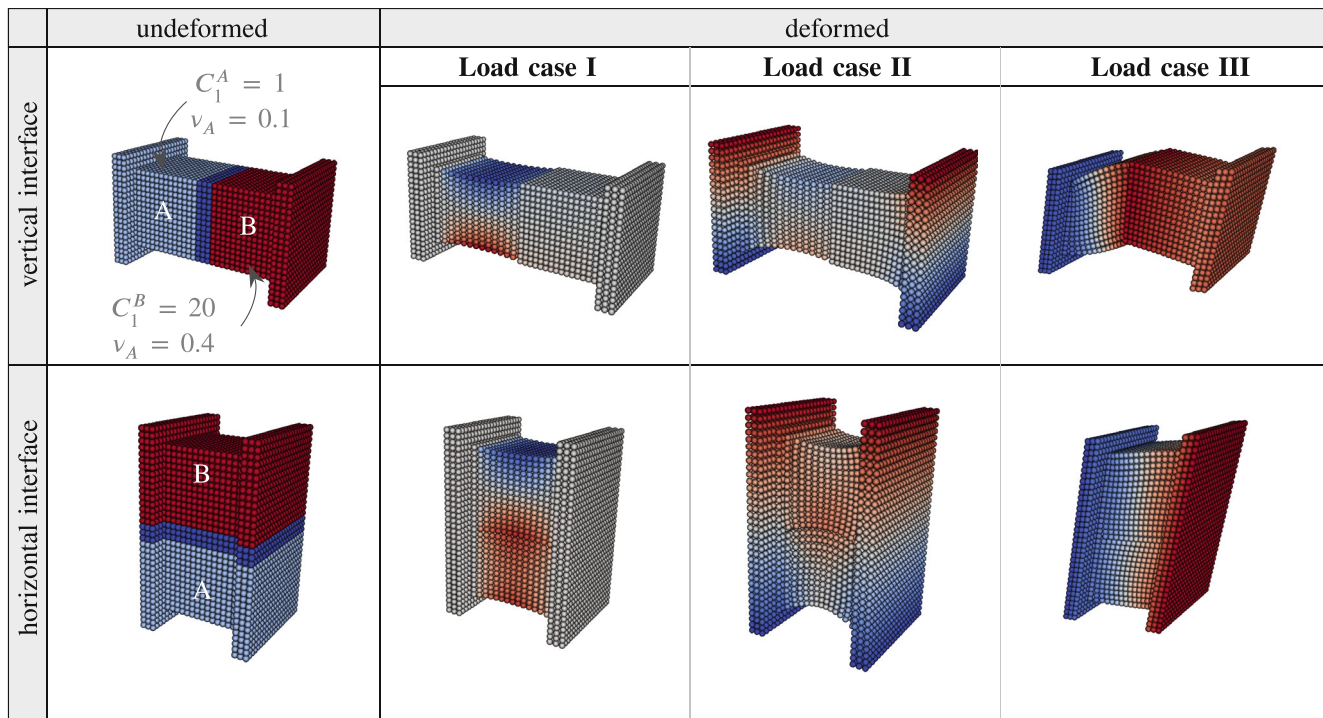
FIGURE 12   Undeformed configurations (left) and deformed configurations (right) of a unit square with different interface geometries at 100 % extension. The color code in the deformed configurations refers to the horizontal and vertical displacement, respectively. The deformations are not magnified

TABLE 3   Convergence rate of the Newton–Raphson algorithm at different load steps corresponding to different levels of extension

1 %	25 %	50 %	75 %	100 %
1	1	1	1	1
4.30e-02	3.63e-02	3.78e-02	5.06e-02	7.12e-02
2.95e-04	1.41e-04	1.71e-04	7.51e-03	7.16e-03
3.07e-08	3.20e-09	9.98e-09	6.37e-06	8.13e-06
3.42e-14	4.46e-14	5.14e-14	1.18e-11	4.42e-11

Note: The L_2-norm of the residual is shown for every iteration. The values are normalized to the norm of the residual at the first iteration.

FIGURE 13 Deformed configurations of three-dimensional domains comprising material A (blue) and material B (red) differing in stiffness and in Poisson's ratio. The color code refers to the displacement in vertical direction. The deformation is magnified for the sake of visualization

5 | CONCLUSION

In the literature, there is no consent on how to treat material discontinuities in PD models. A common technique is to determine separate interfacial material parameters. However, there is no agreement on an appropriate mixture rule. In this article, we propose a novel approach for nonlocal modeling of material interfaces that is in harmony with the spirit of PD and offers a meaningful and unique alternative to existing methods. In an extended interface the material domains overlap and are kinematically bonded to each other. The computation of the interaction forces in the two domains are decoupled from each other, whereby the use of the material parameters is straightforward and introducing a mixture rule is no longer required. In this work, due to its promising features, we employ CPD, recently established by Javili et al.[16] However, we point out that the presented approach is generic and not restricted to CPD.

In the scope of this contribution, the concept of a kinematically coupled interface is elaborated on and a detailed description of the implementation within a CPD framework is provided. The methodology is numerically tested on a variety of two-dimensional bimaterial interfaces under different loading conditions and for different material characteristics. We validate our model by carrying out a nonlocality study, which shows convergence to a local model for decreasing horizon sizes. We illustrate that even at large deformations, the presence of an interface does not impair the excellent convergence behavior of the solution method. Moreover, the applicability of the proposed model to three-dimensional problems is demonstrated. Altogether, our method has shown the potential for modeling nonlocal bimaterial interfaces in a simple manner and sets the stage for the use of CPD in application areas involving heterogeneous materials.

CONFLICT OF INTEREST
The authors declare no potential conflict of interests.

ORCID

Marie Laurien https://orcid.org/0000-0003-1691-0263
Ali Javili https://orcid.org/0000-0001-7965-7088
Paul Steinmann https://orcid.org/0000-0003-1490-947X

REFERENCES

1. Silling SA. Reformulation of elasticity theory for discontinuities and long-range forces. *J Mech Phys Solids*. 2000;48(1):175-209. doi:10.1016/S0022-5096(99)00029-0
2. Javili A, Morasata R, Oterkus E, Oterkus S. Peridynamics review. *Math Mech Solids*. 2019;24(11):3714-3739. doi:10.1177/1081286518803411
3. Askari E, Bobaru F, Lehoucq R, Parks M, Silling S, Weckner O. Peridynamics for multiscale materials modeling. *J Phys Conf Ser*. 2008;125:012078.
4. Bobaru F, Ha YD. Adaptive refinement and multiscale modeling in 2D peridynamics. *Int J Multisc Comput Eng*. 2011;9(6):635-660. doi:10.1615/IntJMultCompEng.2011002793
5. Ebrahimi S, Steigmann D, Komvopoulos K. Peridynamics analysis of the nanoscale friction and wear properties of amorphous carbon thin films. *J Mech Mater Struct*. 2015;10(5):559-572. doi:10.2140/jomms.2015.10.559
6. Madenci E, Barut A, Phan ND. Peridynamic unit cell homogenization. Proceedings of the 58th AIAA/ASCE/AHS/ASC Structures, Structural Dynamics, and Materials Conference; 2017; AIAA SciTech Forum, Grapevine, TX
7. Xia W, Oterkus E, Oterkus S. Ordinary state-based peridynamic homogenization of periodic micro-structured materials. *Theor Appl Fract Mech*. 2021;113:102960. doi:10.1016/j.tafmec.2021.102960
8. Oterkus S, Madenci E, Agwai A. Fully coupled peridynamic thermomechanics. *J Mech Phys Solids*. 2014;64:1-23. doi:10.1016/j.jmps.2013.10.011
9. Oterkus S, Madenci E, Agwai A. Peridynamic thermal diffusion. *J Comput Phys*. 2014;265:71-96. doi:10.1016/j.jcp.2014.01.027
10. Oterkus S. *Peridynamics for the Solution of Multiphysics Problems*. PhD thesis. University of Arizona; 2015.
11. Lejeune E, Linder C. Modeling tumor growth with peridynamics. *Biomech Model Mechanobiol*. 2017;16(4):1141-1157. doi:10.1007/s10237-017-0876-8
12. Lejeune E, Linder C. Interpreting stochastic agent-based models of cell death. *Comput Methods Appl Mech Eng*. 2020;360:112700. doi:10.1016/j.cma.2019.112700
13. Schaller E, Javili A, Schmidt I, Papastavrou A, Steinmann P. A peridynamic formulation for nonlocal bone remodelling. *Comput Methods Biomech Biomed Eng*. 2022.
14. Schaller E, Javili A, Steinmann P. Open system peridynamics; 2022. Manuscript submitted for publication.
15. Silling SA, Epton M, Weckner O, Xu J, Askari E. Peridynamic states and constitutive modeling. *J Elast*. 2007;88(2):151-184. doi:10.1007/s10659-007-9125-1
16. Javili A, McBride A, Steinmann P. Continuum-kinematics-inspired peridynamics. Mechanical problems. *J Mech Phys Solids*. 2019;131:125-146. doi:10.1016/j.jmps.2019.06.016
17. Silling SA. Stability of peridynamic correspondence material models and their particle discretizations. *Comput Methods Appl Mech Eng*. 2017;322:42-57. doi:10.1016/j.cma.2017.03.043
18. Javili A, Firooz S, McBride AT, Steinmann P. The computational framework for continuum-kinematics-inspired peridynamics. *Comput Mech*. 2020;66(4):795-824. doi:10.1007/s00466-020-01885-3
19. Javili A, Ekiz E, McBride A, Steinmann P. Continuum-kinematics-inspired peridynamics: thermo-mechanical problems. *Contin Mech Thermodyn*. 2021;1-25. doi:10.1007/s00161-021-01000-8
20. Javili A, McBride A, Mergheim J, Steinmann P. Towards elasto-plastic continuum-kinematics-inspired peridynamics. *Comput Methods Appl Mech Eng*. 2021;380:113809. doi:10.1016/j.cma.2021.113809
21. Javili A, McBride AT, Steinmann P. A geometrically exact formulation of peridynamics. *Theor Appl Fract Mech*. 2021;111:102850. doi:10.1016/j.tafmec.2020.102850
22. Ekiz E, Steinmann P, Javili A. Relationships between the material parameters of continuum-kinematics-inspired peridynamics and isotropic linear elasticity for two-dimensional problems. *Int J Solids Struct*. 2022;238:111366. doi:10.1016/j.ijsolstr.2021.111366
23. Zhou XP, Tian DL. A novel linear elastic constitutive model for continuum-kinematics-inspired peridynamics. *Comput Methods Appl Mech Eng*. 2021;373:113479. doi:10.1016/j.cma.2020.113479
24. Tian DL, Zhou XP. A continuum-kinematics-inspired peridynamic model of anisotropic continua: elasticity, damage, and fracture. *Int J Mech Sci*. 2021;199:106413. doi:10.1016/j.ijmecsci.2021.106413
25. Cheng Z, Zhang G, Wang Y, Bobaru F. A peridynamic model for dynamic fracture in functionally graded materials. *Compos Struct*. 2015;133:529-546. doi:10.1016/j.compstruct.2015.07.047
26. Cheng Z, Sui Z, Yin H, Feng H. Numerical simulation of dynamic fracture in functionally graded materials using peridynamic modeling with composite weighted bonds. *Eng Anal Bound Elem*. 2019;105:31-46. doi:10.1016/j.enganabound.2019.04.005
27. Tan Y, Liu Q, Zhang L, Liu L, Lai X. Peridynamics model with surface correction near insulated cracks for transient heat conduction in functionally graded materials. *Materials*. 2020;13(6):1340. doi:10.3390/ma13061340
28. Ozdemir M, Kefal A, Imachi M, Tanaka S, Oterkus E. Dynamic fracture analysis of functionally graded materials using ordinary state-based peridynamics. *Compos Struct*. 2020;244:112296. doi:10.1016/j.compstruct.2020.112296

29. Laurien M, Javili A, Steinmann P. Nonlocal wrinkling instabilities in bilayered systems using peridynamics. *Comput Mech*. 2021;68(5):1023-1037. doi:10.1007/s00466-021-02057-7

30. Alali B, Gunzburger M. Peridynamics and material interfaces. *J Elast*. 2015;120(2):225-248. doi:10.1007/s10659-014-9512-3

31. Seleson P, Gunzburger M, Parks ML. Interface problems in nonlocal diffusion and sharp transitions between local and nonlocal domains. *Comput Methods Appl Mech Eng*. 2013;266:185-204. doi:10.1016/j.cma.2013.05.018

32. Capodaglio G, D'Elia M, Bochev P, Gunzburger M. An energy-based coupling approach to nonlocal interface problems. *Comput Fluids*. 2020;207:104593. doi:10.1016/j.compfluid.2020.104593

33. Griebel M, Knapek S, Zumbusch G. *Numerical Simulation in Molecular Dynamics: Numerics, Algorithms, Parallelization, Applications*. Springer; 2007.

34. Heinecke A, Eckhardt W, Horsch M, Bungartz H. *Supercomputing for Molecular Dynamics Simulations: Handling Multi-Trillion Particles in Nanofluidics*. Springer International Publishing; 2015.

35. Wang F, Liu L, Liu Q, Cao D, Yang S. Studies of bimaterial interface fracture with peridynamics. Proceedings of the 2015 International Power, Electronics and Materials Engineering Conference; 2015:856-861; Atlantis Press.

36. Alebrahim R. Peridynamic modeling of lamb wave propagation in bimaterial plates. *Compos Struct*. 2019;214:12-22. doi:10.1016/j.compstruct.2019.01.108

37. Behera D, Roy P, Madenci E. Peridynamic modeling of bonded-lap joints with viscoelastic adhesives in the presence of finite deformation. *Comput Methods Appl Mech Eng*. 2021;374:113584. doi:10.1016/j.cma.2020.113584

38. Diyaroglu C, Oterkus S, Oterkus E, Madenci E. Peridynamic modeling of diffusion by using finite-element analysis. *IEEE Trans Compon Packag Manuf Technol*. 2017;7(11):1823-1831. doi:10.1109/TCPMT.2017.2737522

39. Rahimi MN, Kefal A, Yildiz M. An improved ordinary-state based peridynamic formulation for modeling FGMs with sharp interface transitions. *Int J Mech Sci*. 2021;197:106322. doi:10.1016/j.ijmecsci.2021.106322

40. Liao Y, Liu L, Liu Q, Lai X, Assefa M, Liu J. Peridynamic simulation of transient heat conduction problems in functionally gradient materials with cracks. *J Therm Stresses*. 2017;40(12):1484-1501. doi:10.1080/01495739.2017.1358070

41. Ahmadi M, Sadighi M, Toudeshky HH. Computational microstructural model of ordinary state-based peridynamic theory for damage mechanisms, void nucleation, and propagation in DP600 steel. *Eng Fract Mech*. 2021;247:107660. doi:10.1016/j.engfracmech.2021.107660

42. Kilic B, Madenci E. An adaptive dynamic relaxation method for quasi-static simulations using the peridynamic theory. *Theor Appl Fract Mech*. 2010;53(3):194-204. doi:10.1016/j.tafmec.2010.08.001

43. Nguyen HA, Wang H, Tanaka S, Oterkus S, Oterkus E. An in-depth investigation of bimaterial interface modeling using ordinary state-based peridynamics. *J Peridyn Nonlocal Model*. 2021;1-27. doi:10.1007/s42102-021-00058-x

44. Bobaru F, Yang M, Alves LF, Silling SA, Askari E, Xu J. Convergence, adaptive refinement, and scaling in 1D peridynamics. *Int J Numer Methods Eng*. 2009;77(6):852-877. doi:10.1002/nme.2439

45. Bobaru F, Foster JT, Geubelle PH, Silling SA. *Handbook of Peridynamic Modeling*. CRC Press; 2016.

APPENDIX A. TANGENT STIFFNESS MATRIX

The expressions for the discretized point-wise tangent stiffness matrix utilized in the Newton–Raphson scheme in Section 3.2 can be derived analytically and are given below. For an extensive derivation we refer to Javili et al.[18] Here, the stiffness matrix $\mathbb{K}^{\bullet\circ}$ is written in a general form for two points $\mathcal{P}^{\bullet}$ and $\mathcal{P}^{\circ}$ with $\{\bullet\circ\} = \{a\alpha, b\beta\}$. It reads

$$\mathbb{K}^{\bullet\circ} = \mathbb{K}_1^{\bullet\circ} + \mathbb{K}_2^{\bullet\circ} + \mathbb{K}_3^{\bullet\circ} \tag{A1}$$

with the contributions from one-, two-, and three-neighbor interactions as follows:

$$\mathbb{K}_1^{\bullet\circ} = \frac{\partial \mathbb{R}_1^{\bullet}}{\partial \mathbb{x}^{\circ}} = \sum_{\substack{i=1 \\ i\neq\bullet}}^{\#\mathcal{N}} C_1^{\bullet} \left[\delta^{io} - \delta^{\bullet\circ} \right] \left[\frac{1}{|\xi^{|}|^3} \xi^{|} \otimes \xi^{|} + \left[\frac{1}{|\Xi^{|}|} - \frac{1}{|\xi^{|}|} \right] \mathbf{i} \right] V_1, \tag{A2}$$

$$\mathbb{K}_2^{\bullet\circ} = \frac{\partial \mathbb{R}_2^{\bullet}}{\partial \mathbb{x}^{\circ}} = \sum_{\substack{i=1 \\ i\neq\bullet}}^{\#\mathcal{N}} \sum_{\substack{j=1 \\ j\neq i \\ j\neq\bullet}}^{\#\mathcal{N}} 2C_2^{\bullet} \left[\delta^{io} - \delta^{\bullet\circ} \right] \frac{1}{|\xi^{|} \times \xi^{||}|^3} \left[[\xi^{||} \cdot \xi^{|}]\xi^{||} - [\xi^{||} \cdot \xi^{||}]\xi^{|} \right] \otimes \left[[\xi^{||} \cdot \xi^{|}]\xi^{||} - [\xi^{||} \cdot \xi^{||}]\xi^{|} \right] V_2$$

$$+ \sum_{\substack{i=1 \\ i\neq\bullet}}^{\#\mathcal{N}} \sum_{\substack{j=1 \\ j\neq i \\ j\neq\bullet}}^{\#\mathcal{N}} 2C_2^\bullet \left[\delta^{io} - \delta^{\bullet\circ}\right] \left[\frac{1}{|\xi^| \times \xi^{||}|} - \frac{1}{|\Xi^| \times \Xi^{||}|}\right] \left[\xi^{||} \otimes \xi^{||} - [\xi^{||} \cdot \xi^{||}]\mathbf{i}\right] V_2$$

$$+ \sum_{\substack{i=1 \\ i\neq\bullet}}^{\#\mathcal{N}} \sum_{\substack{j=1 \\ j\neq i \\ j\neq\bullet}}^{\#\mathcal{N}} 2C_2^\bullet \left[\delta^{jo} - \delta^{\bullet\circ}\right] \frac{1}{|\xi^| \times \xi^{||}|^3} \left[[\xi^{||} \cdot \xi^|]\xi^{||} - [\xi^| \cdot \xi^{||}]\xi^|\right] \otimes \left[[\xi^| \cdot \xi^{||}]\xi^| - [\xi^| \cdot \xi^|]\xi^{||}\right] V_2$$

$$+ \sum_{\substack{i=1 \\ i\neq\bullet}}^{\#\mathcal{N}} \sum_{\substack{j=1 \\ j\neq i \\ j\neq\bullet}}^{\#\mathcal{N}} 2C_2^\bullet \left[\delta^{jo} - \delta^{\bullet\circ}\right] \left[\frac{1}{|\xi^| \times \xi^{||}|} - \frac{1}{|\Xi^| \times \Xi^{||}|}\right] \left[\xi^{||} \otimes \xi^| + [\xi^{||} \cdot \xi^|]\mathbf{i} - 2\xi^| \otimes \xi^{||}\right] V_2, \tag{A3}$$

$$\mathbb{K}_3^{\bullet\circ} = \frac{\partial \mathbb{R}_3^\bullet}{\partial \mathbf{x}^\circ}$$

$$= \sum_{\substack{i=1 \\ i\neq\bullet}}^{\#\mathcal{N}} \sum_{\substack{j=1 \\ j\neq i \\ j\neq\bullet}}^{\#\mathcal{N}} \sum_{\substack{k=1 \\ k\neq j \\ k\neq i \\ k\neq\bullet}}^{\#\mathcal{N}} 3C_3^\bullet \left[\delta^{io} - \delta^{\bullet\circ}\right] \frac{1}{|[\Xi^| \times \Xi^{||}] \cdot \Xi^{|||}|} \left[[\xi^{||} \times \xi^{|||}] \otimes [\xi^{||} \times \xi^{|||}]\right] V_3$$

$$+ \sum_{\substack{i=1 \\ i\neq\bullet}}^{\#\mathcal{N}} \sum_{\substack{j=1 \\ j\neq i \\ j\neq\bullet}}^{\#\mathcal{N}} \sum_{\substack{k=1 \\ k\neq j \\ k\neq i \\ k\neq\bullet}}^{\#\mathcal{N}} 3C_3^\bullet \left[\delta^{jo} - \delta^{\bullet\circ}\right] \left[\frac{1}{|[\Xi^| \times \Xi^{||}] \cdot \Xi^{|||}|} - \frac{1}{|[\xi^| \times \xi^{||}] \cdot \xi^{|||}|}\right] \left[[\xi^| \times \xi^{||}] \cdot \xi^{|||}\right] \left[\varepsilon \cdot \xi^{|||}\right] V_3$$

$$+ \sum_{\substack{i=1 \\ i\neq\bullet}}^{\#\mathcal{N}} \sum_{\substack{j=1 \\ j\neq i \\ j\neq\bullet}}^{\#\mathcal{N}} \sum_{\substack{k=1 \\ k\neq j \\ k\neq i \\ k\neq\bullet}}^{\#\mathcal{N}} 3C_3^\bullet \left[\delta^{jo} - \delta^{\bullet\circ}\right] \frac{1}{|[\Xi^| \times \Xi^{||}] \cdot \Xi^{|||}|} \left[[\xi^{||} \times \xi^{|||}] \otimes [\xi^{|||} \times \xi^|]\right] V_3$$

$$- \sum_{\substack{i=1 \\ i\neq\bullet}}^{\#\mathcal{N}} \sum_{\substack{j=1 \\ j\neq i \\ j\neq\bullet}}^{\#\mathcal{N}} \sum_{\substack{k=1 \\ k\neq j \\ k\neq i \\ k\neq\bullet}}^{\#\mathcal{N}} 3C_3^\bullet \left[\delta^{ko} - \delta^{\bullet\circ}\right] \left[\frac{1}{|[\Xi^| \times \Xi^{||}] \cdot \Xi^{|||}|} - \frac{1}{|[\xi^| \times \xi^{||}] \cdot \xi^{|||}|}\right] \left[[\xi^| \times \xi^{||}] \cdot \xi^{|||}\right] \left[\varepsilon \cdot \xi^{||}\right] V_3$$

$$+ \sum_{\substack{i=1 \\ i\neq\bullet}}^{\#\mathcal{N}} \sum_{\substack{j=1 \\ j\neq i \\ j\neq\bullet}}^{\#\mathcal{N}} \sum_{\substack{k=1 \\ k\neq j \\ k\neq i \\ k\neq\bullet}}^{\#\mathcal{N}} 3C_3^\bullet \left[\delta^{ko} - \delta^{\bullet\circ}\right] \frac{1}{|[\Xi^| \times \Xi^{||}] \cdot \Xi^{|||}|} \left[[\xi^{||} \times \xi^{|||}] \otimes [\xi^| \times \xi^{||}]\right] V_3 . \tag{A4}$$

Here, $\mathbf{i}$ is the identity tensor.